BIOMEDICAL MATERIALS

A method for single-neuron chronic recording from the retina in awake mice

Guosong Hong[1]*, Tian-Ming Fu[1]*, Mu Qiao[2]*, Robert D. Viveros[3], Xiao Yang[1], Tao Zhou[1], Jung Min Lee[1,4], Hong-Gyu Park[1,4], Joshua R. Sanes[2], Charles M. Lieber[1,3]†

The retina, which processes visual information and sends it to the brain, is an excellent model for studying neural circuitry. It has been probed extensively ex vivo but has been refractory to chronic in vivo electrophysiology. We report a nonsurgical method to achieve chronically stable in vivo recordings from single retinal ganglion cells (RGCs) in awake mice. We developed a noncoaxial intravitreal injection scheme in which injected mesh electronics unrolls inside the eye and conformally coats the highly curved retina without compromising normal eye functions. The method allows 16-channel recordings from multiple types of RGCs with stable responses to visual stimuli for at least 2 weeks, and reveals circadian rhythms in RGC responses over multiple day/night cycles.

As an approachable part of the brain, the retina provides an excellent model for analyzing the assembly and function of information-processing circuits in the central nervous system (CNS) (*1*, *2*). Interneurons receive signals from light-sensitive photoreceptors (rods and cones) and pass it to retinal ganglion cells (RGCs), which send axons through the optic nerve to visual areas of the brain. Whereas photoreceptors are akin to pixels, information processing by interneurons renders each of ≥40 types of RGCs selectively responsive to specific visual features such as motion or color contrasts (*2*–*4*). However, whereas in vivo single-neuron recordings in awake, behaving animals are routine for many parts of the brain (*5*, *6*), analysis of RGCs has relied primarily on ex vivo electrophysiological recording (*7*, *8*) and calcium imaging (*4*). Although these ex vivo studies have provided deep insights into retinal computations, they are limited in several respects. First, systemic effects such as neuromodulation, alterations in hormonal milieu, and circadian variation are difficult to study ex vivo (*9*–*12*). Second, recordings are limited to the short lifetime of the preparation, typically a few hours, so their ability to detect plasticity in activity patterns is compromised. Third, rod function is prone to rapid loss in explants, partly because of its dependence on pigment epithelium, which is generally removed during explantation. Therefore, ex vivo recordings of rod activities over extended times have remained challenging (*4*). Finally, it is obviously infeasible to correlate retinal activity ex vivo with organismic responses or behaviors. In vivo RGC electrophysiology could offer insight into the interaction between the retina and related brain regions involved in vision processing and regulation (*9*, *13*–*15*), yet existing technologies either have been unable to achieve recordings at single-RGC resolution in mice (*11*) or have been limited to one or two channels of acute recording in anesthetized animals with larger eyes (*16*, *17*).

We report chronically stable in vivo recordings from functionally diverse RGCs in awake mice using epiretinal-implanted mesh electronics delivered via noncoaxial and minimally invasive intravitreal injection to form a chronically stable conformal retina interface. We designed a 16-channel mesh electronics probe with recording electrodes distributed evenly over a 1.5 mm × 0.8 mm region in four parallel rows to ensure coverage and interrogation of a large area of the retina after injection. The 16 recording electrodes (Fig. 1A, I, green arrow) are individually addressable through polymer-encapsulated metal interconnect lines that terminate at input/output (I/O) pads (Fig. 1A, I, red arrow), which provide connection to external recording instrumentation. The tissue-like mesh electronics probes were fabricated using standard photolithography (*18*–*22*), with ~90% porosity in two dimensions and mesh ribbon element widths of ≤10 μm to facilitate syringe injection through capillary needles and to minimize interference with the retina.

The three-dimensional highly concave mouse retina precludes using conventional methods, such as silicon, glass, or metal electrodes (*7*, *16*, *23*) or planar microelectrode arrays (*8*), to form a conformal and chronically stable retina interface.

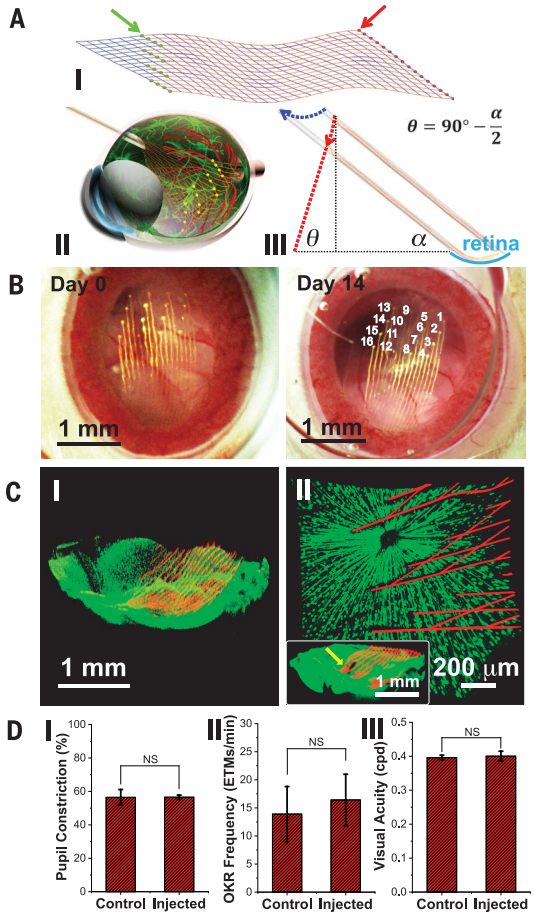

Fig. 1. Noncoaxial intravitreal injection and conformal coating of mesh electronics on the mouse retina. (**A**) I: Schematic showing the layout of mesh electronics comprising 16 recording electrodes (green dots indicated by a green arrow) and I/O pads (red dots indicated by a red arrow). II: Schematic showing noncoaxial intravitreal injection of mesh electronics onto the RGC layer. Multiplexed recording electrodes are shown as yellow dots. III: Schematic of noncoaxial injection that allows controlled positioning of mesh electronics on the concave retina surface (cyan arc). The blue and red dotted arrows indicate the motion of the needle and desired trajectory of the top end of the mesh, respectively (see fig. S1 for details) (*22*). (**B**) In vivo through-lens images of the same mouse eye fundus on days 0 and 14 after injection of mesh electronics, with electrode indexing in the day 14 image (*22*). (**C**) Ex vivo imaging of the interface between injected mesh electronics (red, mesh polymer elements) and the retina (green dots, RGCs) on days 0 (I) and 7 (II) after injection. The inset of II shows the region indicated by a yellow arrow where the high-resolution image was taken (*22*). (**D**) Comparison of pupillary reflex ($n = 3$), OKR ($n = 5$), and visual acuity ($n = 3$) between control and injected mouse eyes. Error bars denote SD; NS, not significant ($P > 0.05$) by one-way ANOVA test.

[1]Department of Chemistry and Chemical Biology, Harvard University, Cambridge, MA, USA. [2]Center for Brain Science and Department of Molecular and Cellular Biology, Harvard University, Cambridge, MA, USA. [3]John A. Paulson School of Engineering and Applied Sciences, Harvard University, Cambridge, MA, USA. [4]Department of Physics, Korea University, Seoul, Republic of Korea.
*These authors contributed equally to this work.
†Corresponding author. Email: cml@cmliris.harvard.edu

Therefore, we asked whether the unique unrolling/unfolding capability of mesh electronics in aqueous solutions (*19*) could occur in the vitreous humor of the eye, which has a very low Young's modulus (*24*). This scheme could enable delivery of a large mesh (>1 mm^2) through a much smaller nonsurgical injection hole (<0.1 mm^2). To deliver the mesh electronics into a mouse eye and form a conformal interface, we developed a controlled noncoaxial injection scheme (Fig. 1A, II and III) with several key features. First, the intravitreal injection procedure is compatible with standard stereotaxic frames commonly used for brain probe implantation (fig. S1, A and B). Second, the ultraflexibility of mesh electronics enables loading and controlled injection into the eye through the lateral canthus, using a small (outer diameter 330 μm) glass capillary needle (fig. S1B and fig. S2, A and B, blue arrows) that is similar in diameter to 29-gauge needles commonly used for intraocular injection of virus vectors and drugs (*25*). Third, synchronizing the volumetric flow with the lateral motion of the needle to follow the curvature of the retina affords lateral positioning and conformal coating of mesh electronics onto the concave retina surface (Fig. 1A, III, fig. S1C, and fig. S3). After injection and needle withdrawal, the mesh was glued externally (fig. S2, C and D) (*22*) and the I/O pads were connected to an interface cable (flexible flat cable), which was mounted on top of the skull, for electrical recording (*20*). The demonstrated injection of mesh electronics into the mouse eye represents a challenging case because of its small size and large curvature; we expect that this method could be readily adapted for animals with larger and less curved eyes, including nonhuman primates.

To verify that the mesh electronics, which is elastically strained when loaded into the capillary needle (*19*), unrolled from the capillary to cover the retina after noncoaxial intravitreal injection, we devised a method for noninvasive in vivo through-lens imaging based on a liquid Hruby lens (Fig. 1B and fig. S4) (*22*). Mesh electronics and retinal vasculature were both visualized from day 0 to day 14 after injection. Quantitative analysis of the locations of representative recording electrodes demonstrated minimal variation of electrode positions over 14 days (table S1) (*22*). We also performed confocal microscopic imaging of the mesh-retina interface after dissection of mesh-injected eyes from TYW3 transgenic mice in which a subset of RGCs was labeled with yellow fluorescent protein (YFP) (*26*) on day 0 and day 7 after injection. Images (Fig. 1C, I) (*22*) showed that the mesh conformed to the concave structure of the retina with a mean distance of 51 ± 35 μm (mean ± SD) between an electrode and the closest labeled RGC. Given that only 10% of RGCs are labeled in the TYW3 mouse retina (*27*), the nearest RGC is likely closer than this mean distance. Higher-resolution images (Fig. 1C, II) further showed that the average soma diameter of RGCs, 12.2 ± 1.9 μm (mean ± SD), was similar to the 10-μm width of mesh elements, and the density of labeled RGCs, 353 cells/mm^2, was within the reported range of 200 to 400 cells/mm^2

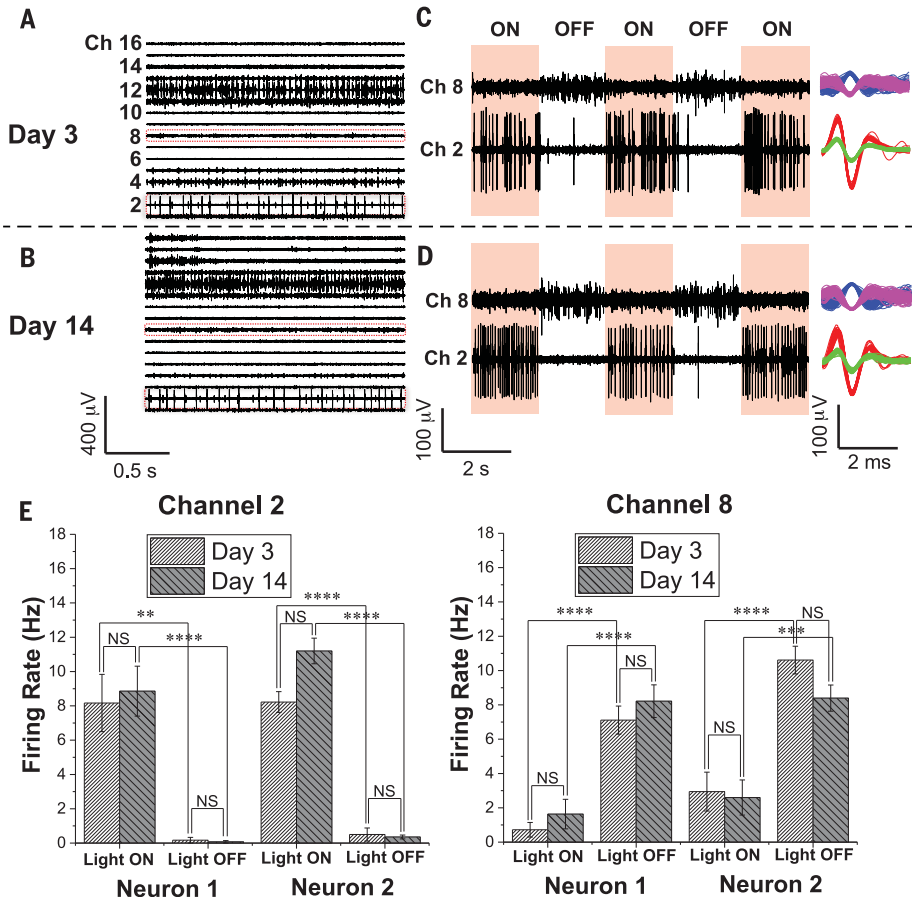

Fig. 2. Chronic 16-channel in vivo electrophysiology of single RGCs measured with mesh electronics. (**A** and **B**) Representative 16-channel recordings from the same mesh electronics delivered onto a mouse retina on day 3 (A) and day 14 (B) after injection. (**C** and **D**) Light modulation of two representative channels (Ch2 and Ch8) in red dashed boxes in (A) and (B) on day 3 (C) and day 14 (D) after injection. The red shaded and unshaded regions indicate the light ON and OFF phases, respectively. Representative sorted spikes assigned to different neurons on both days are shown in the rightmost column for each channel. Each distinct color in the sorted spikes represents a unique identified neuron. (**E**) Firing rates of all sorted neurons from Ch2 and Ch8 during light modulations on days 3 and 14 after injection (*22*). Error bars denote SEM. $^{**}P < 0.01$, $^{***}P < 0.001$, $^{****}P < 0.0001$ (one-way ANOVA); NS, not significant ($P > 0.05$). Five mice were used for multiplexed recordings.

for YFP-labeled RGCs in the central retina of TYW3 mice (*27*). Together, the in vivo and ex vivo images confirmed a chronically stable, conformal, and intimate interface between the three-dimensional curved retina and the injected mesh electronics, with no observable perturbation of RGC density or distribution.

Because of the rigidity of conventional probes used for single-channel in vivo retina recording in larger animals, sutures and fixation rings are usually used to suppress the normal motor functions of the eye even when the animals are anesthetized (*16*, *28*). We asked whether we could take advantage of the ultraflexibility of mesh electronics to minimize interference with normal eye functions during recording in awake mice. First, we used near-infrared imaging (*13*) to track eye responses during air puffs. Chronic studies of the blink reflex exhibited immediate and complete responses to timed air puffs (fig. S5A), with no statistically significant difference between mesh-implanted and control eyes (fig. S5C, I). Second, to assess retinal responsiveness to light, we measured the pupillary response as a function of ambient light intensity modulation for control eyes and mesh-injected eyes (fig. S5B and movie S1). We detected prompt and full-scale pupil expansion and shrinkage in response to increases and decreases in brightness, respectively (fig. S5C, II). Quantification of pupil constriction (*22*) revealed no statistically significant difference between control eyes and mesh-injected eyes (Fig. 1D, I). Third, to assess the influence of the injected mesh on normal eye movement, we characterized the optokinetic reflex (OKR) in response to moving gratings (*29*). We observed that the amplitude, temporal pattern, directionality, and speed of the OKR were consistent between the control and mesh-injected eyes (fig. S5D). Quantitative analyses of eye movement frequency showed no statistically significant difference between the mesh-injected and control eyes

(Fig. 1D, II), both of which were also consistent with previous reports (*30*). Last, to evaluate the impact of the injected mesh on visual acuity, we measured the OKR in response to moving gratings with varying spatial frequencies, and found the mesh-injected eyes to exhibit the same visual acuity as the control (~0.4 cycles per degree; Fig. 1D, III) (*31*). It is also noteworthy that the transparent polymer constituting the mesh scaffold with <5% space occupied by metal features yields minimal blockage of incoming light, as evidenced by the ~95% light transmittance in the 400- to 600-nm spectral window visible to the mouse (*32*) (fig. S5C, II, inset), resulting in negligible distortion of visual input. Taken together, these data demonstrate that injection of the mesh electronics causes minimal damage to the orbicularis oculi, iris dilator, and extraocular muscles as well as negligible interference with light perception and visual acuity of the retina.

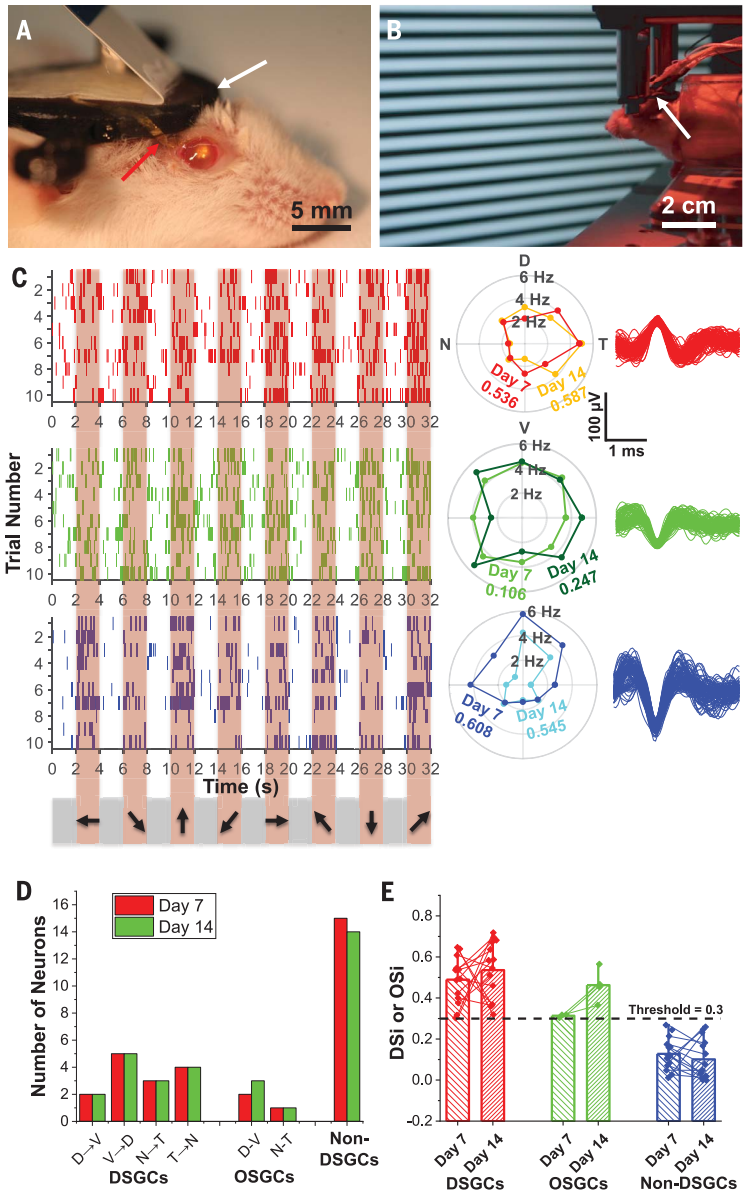

Fig. 3. Chronic in vivo recording and tracking of the same DSGCs. (**A**) Photograph showing a mouse immediately after mesh injection. The red and white arrows indicate part of mesh electronics outside of the eye and a head plate for head fixation, respectively. (**B**) Red-light photograph showing in vivo recording of DSGCs in response to moving grating stimulations (*22*). (**C**) Raster (left), polar plots (center), and overlaid spike waveforms (right) of single-unit firing events of three neurons (with corresponding colors) from Ch8 in response to moving grating stimulations on days 7 and 14 after injection. In the raster plots, the pink shaded regions correspond to times when gratings were displayed on the screen, with moving directions indicated by arrows on the bottom (*22*). Only the raster plots on day 7 are shown. In the polar plots, the DSi for each cell on different days is labeled with corresponding colors. (**D**) Bar chart summarizing numbers of identified DSGCs, OSGCs, and non-DSGCs on day 7 (red bars) and day 14 (green bars) after injection. (**E**) Bar chart with overlaid scatterplot of DSi or OSi of all RGCs on days 7 and 14, with thin lines of corresponding colors connecting the same neurons identified on both days. The bar height and the whisker indicate the mean and maximum of DSi and OSi values, respectively. Four mice were used for direction and orientation selectivity studies; data shown are from one representative mouse.

Having shown that the mesh electronics probe has negligible effect on normal visual functions, we conducted a series of tests to investigate its ability to detect the diverse RGC activities. First, we asked how many of the 16 channels in the implanted probe were sufficiently close to RGCs to record single-unit activity. Figure 2A and fig. S6A show examples from two mice in which we obtained high-quality recordings from all 16 channels, with a signal-to-noise ratio (SNR) of >7 for single-unit spikes. Moreover, single-unit activity was detected in at least 12 channels from each of five separate mice, thus highlighting the robustness of the injected probes for multiplexed retinal electrophysiology.

Second, we asked whether we could record repeatedly from the same sets of RGCs. Multiplexed 16-channel recordings revealed that the SNR from all channels remained >7 for single-unit spikes on days 3 and 14, with little variation in SNR for each specific channel (Fig. 2, A and B, and fig. S7A). The ON/OFF light response in these two representative channels (Ch2 and Ch8; Fig. 2, C and D), which included four RGC neurons (two for each channel) identified by spike sorting, also demonstrated statistically significant differences in modulation of firing patterns (Fig. 2E). Specifically, analysis of variance (ANOVA) showed a statistically significant ($P < 0.01$) difference in firing rate between ON and OFF phases of light modulation, but no significant ($P > 0.05$) difference during the same ON or OFF phase at different days (*22*). Furthermore, analyses of the ON-OFF indices (*4*, *22*) yielded values of 0.97 and 0.91 for the two Ch2 neurons and –0.74 and –0.55 for the two Ch8 neurons; thus, the two Ch2 and two Ch8 neurons can be identified as ON and OFF RGCs, respectively.

Third, we asked whether it was possible to assess the chronic stability and behavior of individual RGCs. We implemented a spike sorting protocol to identify and cluster single units based on principal components analysis (PCA) (*22*, *33*). L-ratio analysis (table S2) (*34*) together with characterization of the number and spike waveforms of detected neurons from all 16 channels on days 3 and 14 (fig. S7B) indicated good unit separation and chronic recording stability. Furthermore, systematic characterization from the two representative channels (Ch2 and Ch8; Fig. 2, C and D, right column) from day 0 through day 14 showed similar average spike waveforms indicative of chronic recording stability (fig. S8A). Moreover, quantitative waveform autocorrelation analyses (fig. S8B) (*35*) showed that the same four neurons were stably tracked across this period. Together, we isolated 134 single units from 89 channels

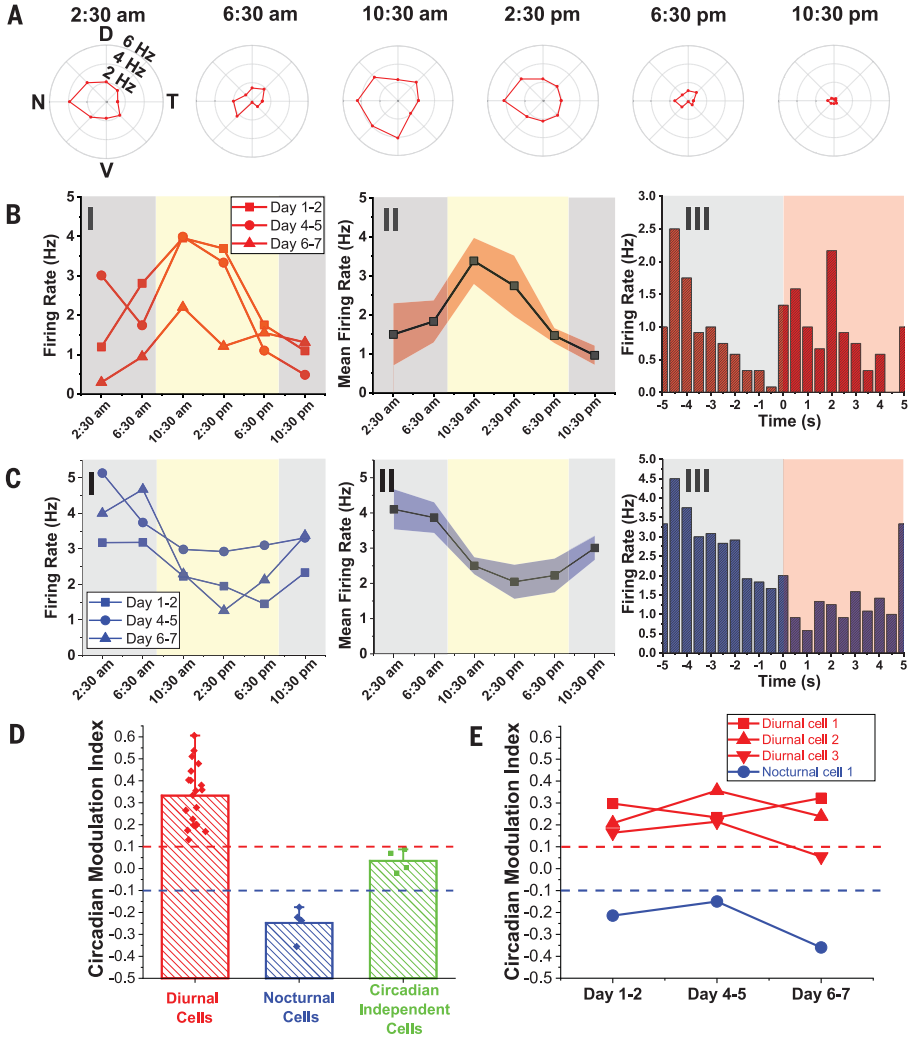

Fig. 4. Chronic circadian modulation of individual RGC activity. (**A**) Representative polar plots of a DSGC at different times in one complete circadian cycle on days 4 and 5 after injection. All graphs are plotted in same range of firing frequencies. (**B**) I: Firing rates of the same DSGC in (A) averaged over preferred directions in three complete circadian cycles on days 1 and 2, 4 and 5, and 6 and 7 after injection. II: Mean firing rate by taking the average over these three circadian cycles. III: This DSGC is identified as an ON-OFF transient type. (**C**) I: Firing rates of another DSGC averaged over preferred directions on three complete circadian cycles on days 1 and 2, 4 and 5, and 6 and 7 after injection. II: Mean firing rate by taking the average over these three circadian cycles. III: This DSGC is identified as an OFF transient type. In (B) and (C), I and II, yellow and gray shaded regions indicate diurnal and nocturnal circadian times, respectively; in (B) and (C), III, the red shaded and white regions indicate light ON and OFF phases, respectively. Red and blue shaded regions in (B) and (C), II, denote SEM. (**D**) Bar chart with overlaid scatterplot of the CMi of diurnal cells (red bars), nocturnal cells (blue bars), and circadian independent cells (green bars) (*22*). The bar height and the whisker indicate the mean and maximum of CMi values, respectively. (**E**) Plots showing the evolution of CMi values for four representative cells (three diurnal cells and one nocturnal cell) that were recorded for three complete circadian cycles. Red and blue dashed lines in (D) and (E) indicate the threshold for defining diurnal and nocturnal cells, respectively. Three mice were used for circadian modulation study of RGC activity.

from five mice with chronic stability; additional examples are described below.

Fourth, to assess the range of RGC types we could detect, we stimulated the retinas in awake mice with a spatially varying grating designed to elicit responses from direction-selective (DS) and orientation-selective (OS) RGCs and investigated the capability to engage the same DS and OS RGCs chronically (*22*). The multiplexed measurements were made with the head rigidly restrained (Fig. 3, A and B, white arrow) to ensure a fixed visual field with respect to the moving grating displayed on a flat screen (movie S2) with alternating 2-s ON and OFF periods (Fig. 3C, pink and white vertical bars). Representative raster plot data from one of these channels on days 7 and 14 (Fig. 3C and fig. S6, B and C) highlight the chronically stable behavior of three spike-sorted RGCs, including spike waveforms, amplitudes, and raster plot responses. Specifically, average spike waveforms for these three neurons in the 10 trials each day, as well as between day 7 and day 14, exhibited minimal systematic change (fig. S9A), which was confirmed by auto- and cross-correlation analyses (fig. S9B). Moreover, polar plots of firing rate versus grating direction (Fig. 3C, middle) showed that these three neurons can be classified as follows: Neuron-1 (red) is a direction-selective ganglion cell (DSGC) with nasal-to-temporal (N→T) preference, neuron-2 (green) is a non-DSGC, and neuron-3 (blue) is a DSGC with ventral-to-dorsal (V→D) preference. The direction preference and selectivity remained stable from day 7 to day 14 after injection, and small variations between days were statistically insignificant (fig. S9, C and D). We note that the intact OKR driven by the moving gratings did not disrupt the chronic RGC recording stability (fig. S10), and that potential OKR-induced random variability was averaged from RGC responses over 10 consecutive trials of moving grating stimulation (*36*).

A summary of our in vivo 16-channel measurements from day 7 to day 14 (Fig. 3D and fig. S11) confirms the stable chronic recording across all channels. Overall, we recorded from 32 RGCs of which 15 were non-DSGCs, 3 were orientation-selective (OSGCs; 2 dorsal-ventral and 1 nasal-temporal), and 14 were DSGCs (2 D→V, 5 V→D, 3 N→T, and 4 T→N) (*22*). The direction selectivity indices (DSi's) and orientation selectivity indices (OSi's) (*22*) remained stable and no RGCs shifted categories between the two recording sessions (days 7 and 14), providing additional evidence that individual cells can be tracked for 2 weeks (Fig. 3E). Moreover, the percentages of DSGCs, OSGCs, and non-DSGCs (44%, 9%, and 47%, respectively) in this dataset are similar to those obtained from recent large-scale calcium imaging of >5000 RGCs in retinal explants (35%, 14.5%, and 51.5%; difference between the two datasets, $P > 0.05$ by χ^2 test) (*4*).

Finally, we asked whether we could use implanted mesh electronics to investigate circadian modulation of RGC activity (*22*). Specifically, we monitored RGCs at 4-hour intervals over several day/night cycles (Fig. 4A) for a total of 18 recordings (nocturnal, 8 p.m. to 8 a.m.; diurnal, 8 a.m. to 8 p.m.). Representative data from a DSGC in a mouse demonstrated that preferred direction and direction selectivity varied little during this period (fig. S12A). In contrast, the absolute firing rate in the preferred direction (±45°) varied in a consistent way over three complete circadian cycles (days 1 and 2, 4 and 5, and 6 and 7 after injection), with a firing rate during the diurnal phase that was on average 77% higher than during the nocturnal phase (Fig. 4B). Similar constancy of preferred direction but circadian variation of activity level was found for other RGCs, including a D→V DSGC and a non-DSGC (fig. S12, B and C).

Overall, of the 28 RGCs from three mice we recorded in this regime, 20 exhibited higher firing rates during the diurnal phase. Four others exhibited decreased firing rates during the diurnal phase, and the remaining four showed minimal circadian modulation, as assessed from their circadian modulation indices (CMi's; Fig. 4, C and D) (*22*). Cells that were tracked for three complete circadian cycles demonstrated that RGCs remained in the same circadian modulation categories, despite slight variations in CMi values (Fig. 4E). Interestingly, of six cells for which ON-OFF preferences were measured carefully, two of three diurnal-high cells were ON and one was ON-OFF, both of the nocturnal-high cells were OFF, and the sole invariant cell was ON-OFF, suggesting a correlation between RGC polarity and day/night modulation of activity that will be interesting to investigate. The pattern of increased diurnal firing activity for the majority of RGCs is consistent with results of a previous ERG study in which the b-wave amplitude, which reflects the population average of ON-bipolar cell activity (*37*), was found to increase in the daytime (*11*).

We have demonstrated multiplexed, chronically stable recording from diverse RGC types by means of syringe-injectable mesh electronics in mice. The ultraflexibility of mesh electronics allowed for nonsurgical intravitreal delivery into mouse eyes via noncoaxial injection and formation of conformal and chronically stable functional interface with the retina in vivo, which can be readily adapted for other animals with larger eyes. This method provides an attractive alternative to past studies of RGC activity in explants and offers important new insights into the dynamic information processing between the retina and other parts of the CNS.

REFERENCES AND NOTES

1. R. H. Masland, *Neuron* **76**, 266–280 (2012).
2. M. Hoon, H. Okawa, L. Della Santina, R. O. Wong, *Prog. Retin. Eye Res.* **42**, 44–84 (2014).
3. J. R. Sanes, R. H. Masland, *Annu. Rev. Neurosci.* **38**, 221–246 (2015).
4. T. Baden *et al*., *Nature* **529**, 345–350 (2016).
5. C. M. Lewis, C. A. Bosman, P. Fries, *Curr. Opin. Neurobiol.* **32**, 68–77 (2015).
6. E. J. Hamel, B. F. Grewe, J. G. Parker, M. J. Schnitzer, *Neuron* **86**, 140–159 (2015).
7. I. J. Kim, Y. Zhang, M. Yamagata, M. Meister, J. R. Sanes, *Nature* **452**, 478–482 (2008).
8. G. D. Field *et al*., *Nature* **467**, 673–677 (2010).
9. T. A. LeGates, D. C. Fernandez, S. Hattar, *Nat. Rev. Neurosci.* **15**, 443–454 (2014).
10. K. S. Korshunov, L. J. Blakemore, P. Q. Trombley, *Front. Cell. Neurosci.* **11**, 91 (2017).
11. C. R. Jackson *et al*., *J. Neurosci.* **32**, 9359–9368 (2012).
12. C. K. Hwang *et al*., *J. Neurosci.* **33**, 14989–14997 (2013).
13. B. H. Liu, A. D. Huberman, M. Scanziani, *Nature* **538**, 383–387 (2016).
14. D. E. Wilson, D. E. Whitney, B. Scholl, D. Fitzpatrick, *Nat. Neurosci.* **19**, 1003–1009 (2016).
15. O. S. Dhande, A. D. Huberman, *Curr. Opin. Neurobiol.* **24**, 133–142 (2014).
16. S. W. Kuffler, *J. Neurophysiol.* **16**, 37–68 (1953).
17. H. B. Barlow, R. M. Hill, W. R. Levick, *J. Physiol.* **173**, 377–407 (1964).
18. T.-M. Fu *et al*., *Nat. Methods* **13**, 875–882 (2016).
19. J. Liu *et al*., *Nat. Nanotechnol.* **10**, 629–636 (2015).
20. G. Hong *et al*., *Nano Lett.* **15**, 6979–6984 (2015).
21. T. Zhou *et al*., *Proc. Natl. Acad. Sci. U.S.A.* **114**, 5894–5899 (2017).
22. See supplementary materials.
23. J. J. Jun *et al*., *Nature* **551**, 232–236 (2017).
24. C. S. Nickerson, H. L. Karageozian, J. Park, J. A. Kornfield, *Invest. Ophthalmol. Vis. Sci.* **45**, 37 (2004).
25. X. Duan *et al*., *Neuron* **85**, 1244–1256 (2015).
26. I. J. Kim, Y. Zhang, M. Meister, J. R. Sanes, *J. Neurosci.* **30**, 1452–1462 (2010).
27. Y. Zhang, I. J. Kim, J. R. Sanes, M. Meister, *Proc. Natl. Acad. Sci. U.S.A.* **109**, E2391–E2398 (2012).
28. N. Suematsu *et al*., *Front. Syst. Neurosci.* **7**, 103 (2013).
29. D. Zoccolan, B. J. Graham, D. D. Cox, *Front. Neurosci.* **4**, 193 (2010).
30. K. Yonehara *et al*., *Neuron* **89**, 177–193 (2016).
31. G. T. Prusky, N. M. Alam, S. Beekman, R. M. Douglas, *Invest. Ophthalmol. Vis. Sci.* **45**, 4611–4616 (2004).
32. G. H. Jacobs *et al*., *Science* **315**, 1723–1725 (2007).
33. R. Q. Quiroga, Z. Nadasdy, Y. Ben-Shaul, *Neural Comput.* **16**, 1661–1687 (2004).
34. N. Schmitzer-Torbert, A. D. Redish, *J. Neurophysiol.* **91**, 2259–2272 (2004).
35. A. Jackson, E. E. Fetz, *J. Neurophysiol.* **98**, 3109–3118 (2007).
36. W. Sun *et al*., *Nat. Neurosci.* **19**, 308–315 (2016).
37. L. Gurevich, M. M. Slaughter, *Vision Res.* **33**, 2431–2435 (1993).

ACKNOWLEDGMENTS

We thank J. E. Dowling for helpful discussions, M. Meister for useful suggestions, and J. Huang for help with recording instrumentation. **Funding:** Supported by Air Force Office of Scientific Research grant FA9550-14-1-0136, Harvard University Physical Sciences and Engineering Accelerator award, and a NIH Director's Pioneer Award 1DP1EB025835-01 (C.M.L.); American Heart Association Postdoctoral Fellowship 16POST27250219 and NIH Pathway to Independence Award from NIA 1K99AG056636-01 (G.H.); a NIH R37 grant from NINDS NS029169 (M.Q. and J.R.S.); and the Harvard University Center for Nanoscale Systems supported by NSF. **Author contributions:** G.H., T.-M.F., M.Q., J.R.S., and C.M.L. designed the experiments; G.H., T.-M.F., M.Q., R.D.V., X.Y., T.Z., J.M.L., and H.-G.P. performed the experiments; G.H., T.-M.F., M.Q., J.R.S., and C.M.L. analyzed the data and wrote the paper; and all authors discussed the results and commented on the manuscript. **Competing interests:** None. **Data and materials availability:** All data are available in the manuscript or the supplementary materials. Mesh electronics probes are available upon request to the authors.

SUPPLEMENTARY MATERIALS

www.sciencemag.org/content/360/6396/1447/suppl/DC1
Materials and Methods
Figs. S1 to S12
Tables S1 and S2
Movies S1 and S2
References (*38*–*44*)

4 January 2018; accepted 26 April 2018
10.1126/science.aas9160